

# ExTraSS: a Domain Decomposed 3D NLTE Radiative Transfer spectral synthesis code for nebular phase transients

Bart F. A. van Baal ,<sup>1</sup>  and Anders Jerkstrand ,<sup>1</sup>

<sup>1</sup>*The Oskar Klein Centre, Department of Astronomy, Stockholm University, AlbaNova, Se-10691 Stockholm, Sweden*

Accepted XXX. Received YYY; in original form ZZZ

## ABSTRACT

In the nebular phase, supernovae are powered by radioactive decay and continuously fade, while their densities have decreased enough such that the expanding nebula becomes (largely) optically thin and the entire structure can be studied. Models for the nebular phase need to take Non-Local Thermodynamic Equilibrium (NLTE) effects into account, while at the same time radiative transfer effects often cannot be ignored. To account for the asymmetric morphologies of SNe, 3D input ejecta models must be used. In this work, we present the ExTraSS (EXplosive TRAnsient Spectral Simulator) code, which has been upgraded to be fully capable of 3D NLTE radiative transfer calculations in order to generate synthetic spectra for explosive transients in the nebular phase, with a focus on supernovae. We solve the long-standing difficulty of 3D NLTE radiative transfer – to manage generation and storage of millions of photoexcitation rates over  $\sim 10^5$  of cells – by developing a new Domain Decomposition algorithm. We describe this new methodology and general code operations in detail, and verify convergence and accuracy.

**Key words:** methods: numerical – software: development – supernovae: general – transients: supernovae

## 1 INTRODUCTION

The main goal of modelling supernova (SN) spectra is to determine key characteristics of the explosion, such as the ejected mass, the composition, and the explosion energy. These can be used to connect back to progenitor systems and obtain information on the explosion mechanism. These modelling efforts come in various flavours of complexity and with different focus points (see [Jerkstrand 2025](#), for a recent review).

One example is codes assuming Local Thermodynamic Equilibrium (LTE) and modelling the outer line forming domain at early phases (e.g. SYNAPPS, [Branch 1980](#); [Thomas et al. 2011](#), the [Mazzali & Lucy 1993](#) code, and TARDIS, [Kerzendorf & Sim 2014](#)). Such codes have the advantage of fast run times and can explore large parameter spaces. More detailed modelling considering certain NLTE effects was also done early in 1D (e.g. [Baron et al. 1995](#); [Hoeflich & Khokhlov 1996](#)). In later phases when LTE breaks down, consideration of a large variety of physical processes, and the full domain, are needed. Much of the initial groundwork to these more complex codes was begun by [Axelrod \(1980\)](#), who outlined the non-thermal and Non-Local Thermodynamic Equilibrium (NLTE) physics needed. Initially, the more complex codes were limited in either more microphysics, or accounting for the multidimensionality of SNe. Nebular-phase (NLTE) codes in 1D were developed by [Fransson & Chevalier \(1989\)](#); [Kozma & Fransson \(1998\)](#); [Mazzali et al. \(2001\)](#), which operated without radiative transfer (in the optically thin limit). Early 2D work of the same type was done by [Maeda et al. \(2006\)](#), in the context of modelling SN 1998bw. The first 3D LTE codes SEDONA ([Kasen et al. 2006](#)) and ARTIS ([Kromer & Sim 2009](#))

slightly predate the second generation of 1D NLTE codes – with radiative transfer – such as SUMO ([Jerkstrand et al. 2011, 2012](#)) and CMFGEN (which was modified for SN modelling by [Hillier & Dessart 2012](#)). Within the more complex codes, large variations still exist on how the spectral synthesis is performed, and which epoch of the SN is studied. Recently, many of these codes were compared by [Blondin et al. \(2022\)](#), which was a collaboration work by the different groups to investigate the level of agreement between their codes for a given input model.

In the days and weeks after the explosion, the SN ejecta are in the so-called “photospheric phase”, where the spectra probe the outer surface layers as optical depths are still high and radiation from deep layers cannot escape. In this phase, many absorption lines are observed, making detailed radiative transfer calculations critical, while the microphysics can be approached in a more simple manner (i.e. in LTE). At late times, the ejecta enter the “nebular phase”, when the ejecta have become (mostly) optically thin and the inner regions are revealed. In this regime, optical depths are smaller, and dominant lines appear in emission rather than absorption. In this regime the radiative transfer becomes simpler to perform, but instead more microphysics (i.e. NLTE) must be accounted for. The transition into the nebular phase has no formally defined time and depends on the expansion velocity and mass of the ejecta, as well as the wavelength as redder emission becomes optically thin more quickly. A more detailed discussion can be found in [Jerkstrand \(2025\)](#).

SNe occur from two distinct progenitor systems: the thermonuclear explosion of (at least one) white dwarf (called Type Ia, SN Ia, see e.g. [Taubenberger 2017](#) for an overview of the many different subtypes), and the core collapse of a massive star (CCSN; stars with  $M_{\text{ZAMS}} \gtrsim 8 M_{\odot}$ , [Heger et al. 2003](#), [Jerkstrand et al. 2026](#)) which encompasses all the other types, depending on what kind of star exploded (see

\* E-mail: barteld.vbaal@astro.su.se

also [Filippenko 1997](#); [Gal-Yam 2017](#)). Multi-dimensional explosion simulations of SNe Ia have been available for quite some time (see [Hillebrandt et al. 2013](#), for a review), and a vast literature on 3D LTE modelling of these exists. NLTE modelling was done in 2D by [Botyánszki et al. \(2018\)](#). [Shingles et al. \(2020\)](#) started working towards including NLTE effects in the 3D code ARTIS, but computed models only in 1D.

In recent years, long-time hydrodynamical modelling of CCSNe has gained pace (e.g. [Wongwathanarat et al. 2015](#); [Stockinger et al. 2020](#); [Gabler et al. 2021](#); [Vartanyan et al. 2025b,a](#)). [Jerkstrand et al. \(2020\)](#) performed the first processing of such a 3D explosion model, computing the deposition and emergence of gamma-ray lines. Spectral synthesis modelling in 3D NLTE began with [van Baal et al. \(2023, 2024\)](#). These works used stripped star input models<sup>1</sup>, which have lower ejecta masses and higher expansion velocities than hydrogen-rich CCSNe, and as such reach homologous expansion faster (but not as fast as SNe Ia). Due to this, their densities in the nebular phase are quite low and radiative transfer impacts are limited. [van Baal et al. \(2023\)](#) worked in a globally optically thin approximation, while [van Baal et al. \(2024\)](#) added an ‘on-the-spot’ treatment for photoionization. For H-rich SNe (such as were modelled by e.g. [Stockinger et al. 2020](#), [Gabler et al. 2021](#) and [Vartanyan et al. 2025b](#)), radiative transfer effects are more important and must be included ([Jerkstrand et al. 2012](#)) – the motivation for the current development work and application to Type II SNe (van Baal et al., submitted).

Including a complete radiative transfer method is computationally much more demanding than the optically thin version of [van Baal et al. \(2023\)](#). The photoexcitation rates alone might require upwards of 1 TB of data to store for a 3D grid with  $\sim 100\,000$  cells, depending on how many elements and excitation levels per ionization stage are used. Even on modern supercomputers, this is not possible to achieve on a single node. As such, for 3D NLTE radiative transfer *domain decomposition* must be pursued, to divide out the computational domain over the compute nodes. While having been developed and used for fission reactor simulations (see e.g. [Alme et al. 2001](#); [Brunner & Brantley 2009](#)), the code version we present in this paper represents, to our knowledge, the first time this has been implemented for a supernova radiative transfer code.

Domain decomposition generally is used for Monte Carlo transport problems which become too large to fit the data for the entire computational grid in the memory of a single core or node ([Alme et al. 2001](#)). Instead, it becomes necessary to break the total grid into smaller subdomains, which reduces how much memory is required to be stored on each node, but which does come with additional communication overhead. The exact form of separation into the subdomains can have strong impacts on the efficiency of the scheme ([Alme et al. 2001](#); [Brunner & Brantley 2009](#)). However, an important question is to what degree transfer occurs between the different subdomains, as high ‘leakage’ rates can lead to large communication costs and non-locality in the computational time ([Siegel et al. 2012](#)).

In this work, we give a complete introduction and description to ExTraSS (EXplosive TRAnsient Spectral Simulator), which was used by [van Baal et al. \(2023, 2024\)](#), with the initial grid structure and  $\gamma$ -ray transport introduced by [Jerkstrand et al. \(2020\)](#). The code has been expanded to include global radiative transfer coupled to photoionization and photoexcitation, which is explained in detail here, alongside the domain decomposition implementation. In a companion

<sup>1</sup> Massive stars can lose their hydrogen envelope e.g. due to interactions with a binary companion, creating ‘stripped stars’. In more extreme cases, even the helium-rich envelope can be lost.

paper (van Baal et al., submitted), the upgraded code is applied to the H-rich  $9.0 M_{\odot}$  model from [Stockinger et al. \(2020\)](#).

The paper is structured as follows: in Section 2, we outline the different components of ExTraSS one by one, starting with the  $\gamma$ -ray transport and finishing with the radiative transfer and domain decomposition. In Section 3 we validate the stability and robustness of ExTraSS in its full form. In Section 4 we explore some alternative approaches to the radiative transfer communication and discuss future code updates. Our conclusion is given in Section 5.

## 2 METHODS

ExTraSS uses a spherical coordinate grid. This has the advantage that cells at larger radii can be made larger while cells at inner radii can be small, enabling us to capture the fine structure at high resolution for the slower-moving ejecta, while retaining efficient transfer at large radii. The robustness of this spherical grid setup versus was shown in detail in [Jerkstrand et al. \(2020\)](#), in Appendix A).

ExTraSS operates in snap-shot mode, meaning photon transport is followed through independent of time. Flight time effects can still be fully included for gamma-ray lines, as well as UVOIR lines if the non-local radiation field is ignored, following the methods of [Jerkstrand et al. \(2020\)](#). For UVOIR lines with global radiative transfer those methods are insufficient, however. This means the code for this application is limited to relatively late phases when optical depths are low enough that the radiation transport time is unimportant.

In order to study the viewing angle impacts, a set of  $20 \times 20$  viewing angles in the polar  $\times$  azimuthal are placed, equally spread along both angles. As ExTraSS is designed with a spherical grid setup, this does mean that the viewers close to the poles (the smallest and largest  $\theta$  angles) are ‘packed’ more closely together, and they each represent a smaller part of the total sky angle. In the optically thin setups, this can be adjusted for as a post-processing step, while in the radiative transport calculations this has to be accounted for at emission, in order to ensure that the emission is sent off isotropically.

In this Section, we will first recap the technical details behind the  $\gamma$ -ray transport ([Jerkstrand et al. 2020](#)), the NLTE solver ([van Baal et al. 2023](#)), and the radiative transport (both the ‘on-the-spot’ photoionization treatment from [van Baal et al. 2024](#), and the full version from van Baal et al., submitted). After this we will discuss the implementation of several memory reduction mechanisms, namely Jagged Arrays and shared memory (introduced to the ExTraSS framework by [van Baal et al. 2023](#)) and then Domain Decomposition (introduced alongside the full Radiative Transfer treatment described here).

### 2.1 $\gamma$ -ray transport

The  $\gamma$ -ray transport was first introduced in [Jerkstrand et al. \(2020\)](#), who described several versions of their 3D photon packet transfer in order to study the radioactive decay lines of the  $\gamma$ -ray field. For the version of ExTraSS presented in this work, these original code setups can still be used, but they have also been integrated into the full 3D NLTE radiative transfer framework in various ways.

The  $\gamma$ -ray transport is as default computed using the ‘Compton scattering mode’, from [Jerkstrand et al. \(2020, Sec 4.6\)](#). In this setting, a total number of packets  $N$  is divided across the cells which contain radioactive material ( $^{56}\text{Ni}$ ,  $^{56}\text{Co}$ ), scaled to the fraction  $f_{\text{cell}}$  of the total  $^{56}\text{Ni}$  that is present in the whole model. Each core then sends a number of  $\gamma$ -ray packets from that cell  $n_{\text{cell},\gamma} = N * f_{\text{cell}}(^{56}\text{Ni})/n_{\text{core}}$ .

Each packet is given a random starting direction by isotropic sampling. For the transfer through the cells, the standard Monte Carlo

formalism with comoving frame energy transformations is applied (e.g. Lucy 2005; Jerkstrand et al. 2011), until scattering occurs. The photoelectric absorption effect is not included as it has negligible impact for energies  $> 68$  keV (Alp et al. 2018), and once a packet drops below 50 keV it will be fully absorbed in the current cell. If a scattering occurs, part of the energy of the packet is lost to the cell where the scattering takes place. Upon scattering, the packets obtain a new travel direction. The reader is referred to Jerkstrand et al. (2020) for more complete details.

For every packet, random numbers are used to choose which of the 47 decay lines the  $^{56}\text{Co}$  will take, consistent with the branching ratios of these lines. Positrons (which carry 3.5% of the energy on average) are assumed to be locally trapped. The  $\gamma$ -ray radiation field  $J_\gamma$  is constructed following the method of Lucy (2005), by following the path the packets traverse through the nebula.

## 2.2 NLTE solver

The NLTE level population solver was first introduced in van Baal et al. (2023) but has been updated and improved since. This NLTE\_SOLVER will solve for the local temperature  $T_{\text{cell}}$  and the NLTE level populations in an iterative manner, holding photoexcitation and photoionization rates fixed. Both thermal and non-thermal physics are accounted for in the solver, alongside impacts from the non-local radiation field. A schematic overview of all the key steps is also shown in Figure 1.

The total number of cells in an ExTraSS model is typically  $\mathcal{O}(10^{5-6})$ , which means that some care has to be taken in the design of the level population solver to keep this computationally feasible (both in run-time and in RAM – see also Sec 2.5). As noted in van Baal et al. (2023), for every ion we include only up to 100 excitation levels, with three ionization stages per element (except H), meaning up to 300 excitation stages are calculated per atomic species. Every atomic species is calculated separately, but the excitation and ionization structures are calculated concurrently in the so-called EXCION\_SOLVER (see also Figure 1). ExTraSS has atomic data sourced from SUMO, currently including H, He, C, O, Ne, Mg, Si, S, Ar, Ca, Ti, Cr, Fe, Co and Ni<sup>2</sup>, meaning up to 15 unique atomic species might be solved for per cell. When atomic data for collision strengths, photoionization cross sections, or recombination rates are missing, the same approximate treatments are done as in SUMO.

As part of the NLTE\_SOLVER, we employ the Spencer-Fano subroutine of Kozma & Fransson (1992) to determine the distribution of the non-thermal electrons from the  $\gamma$ -ray energy deposition (line 14 in Figure 1). In the current version of ExTraSS, all three channels of heating, ionization and excitation are included. As the inclusion of the excitation channel makes the Spencer-Fano calculation computationally expensive, it is only called on the first and fourth (NLTE\_SOLVER) iteration, and every subsequent ten iterations afterwards. Additionally, if all elements except H have reached convergence, it is no longer called<sup>3</sup>. In van Baal et al. (2023) and van Baal et al. (2024), the ex-

<sup>2</sup> These are the elements present in the typical P-HotB long-time simulation models that have been employed as inputs. Elements such as Na and N, which can have lines in the optical in the nebular phase (see e.g. Jerkstrand et al. 2018; Dessart et al. 2021; Barmentlo et al. 2024) have not been included thus far, but could be incorporated in a straight-forward manner.

<sup>3</sup> Tests indicated that occasionally H will take many more iterations in the excitation-ionization solver than other elements, and that subsequent Spencer-Fano calls had no impact on the final solution but did significantly impact the run-time.

$$\begin{bmatrix} 1 & 1 & 1 & 1 & 1 & 1 \\ X_{12} & -T_{22} & X_{32} & R_{42} & R_{52} & R_{62} \\ X_{13} & X_{23} & -T_{33} & R_{43} & R_{53} & R_{63} \\ \Gamma_{14} & \Gamma_{24} & \Gamma_{34} & -T_{44} & X_{54} & X_{64} \\ \Gamma_{15} & \Gamma_{25} & \Gamma_{35} & X_{45} & -T_{55} & X_{65} \\ \Gamma_{16} & \Gamma_{26} & \Gamma_{36} & X_{46} & X_{56} & -T_{66} \end{bmatrix} \begin{bmatrix} n_1 \\ n_2 \\ n_3 \\ n_4 \\ n_5 \\ n_6 \end{bmatrix} = \begin{bmatrix} n_{\text{element}} \\ 0 \\ 0 \\ 0 \\ 0 \\ 0 \end{bmatrix}$$

**Table 1.** A schematic overview of what the matrix constructed by the EXCION\_SOLVER looks like for an atom with two ionization stages (neutral corresponding to levels 1 – 3 and ionized to levels 4 – 6). The subscripts  $ij$  give the flow from state  $i$  to state  $j$ . The diagonal values  $T_{ii}$  contain the sum of outgoing flows from  $i$ , hence the minus sign. X refers to excitation/deexcitation flows,  $\Gamma$  to ionization flows (from neutral to singly ionized in this example) and R to recombination flows (from singly ionized to neutral in this example).  $n_i$  is the vector of current level populations for which the matrix is solved, while on the right-hand side the conservation equation is given together with the first row on the left-hand side. Copied from van Baal et al. (2023) with approval from the authors.

citation channel was not used, and instead the Spencer-Fano routine was called the first two iterations and then every 4th.

For the first global iteration of the NLTE\_SOLVER, there is no radiation field yet to determine photoionization and photoexcitation rates. As such, for this first iteration the ‘on-the-spot’ photoionization approximation from van Baal et al. (2024) is applied (line 15 in Figure 1). In this treatment, emission generated from recombination is used to calculate photoionization rates for the ground state multiplet plus eight next excited states, all under the hydrogenic approximation for the photoionization cross-sections (Rybicki & Lightman 1979). The excess energy due to ionization through this treatment ( $h\nu - I$  per photon, where  $I$  is the ionization potential) is accounted for as an extra heating source when calculating the temperature (and the recombination flows as cooling). This approximation is only applied locally and only for the first global iteration, before any radiation field has been generated. In total, the NLTE\_SOLVER will do up to 150 iterations, during each of which it will call first the level population solver and then the temperature solver.

The maximum number of iterations for each call to EXCION\_SOLVER (solving the populations for all present elements) has been updated to 200 compared to van Baal et al. (2023). In each iteration, the excitation and ionization structure of each atom is solved separately and checked for convergence. For each element, a matrix (see Table 1 for a small example) containing the rates from each level to all other levels is constructed, and a numerical Jacobian is calculated. A Newton-Raphson scheme is used alongside a damping factor to determine the new level populations. The default dampening factor is 0.95, which is reduced to 0.75 after 10 iterations, to 0.5 after 35, to 0.25 after 50 and finally to 0.05 after 90 iterations<sup>4</sup>. An atomic species is considered converged if the difference between the old and new level populations are less than 1% for every state.

Upon the conclusion of the EXCION\_SOLVER, the temperature is solved in the T\_SOLVER, which accounts for bound-bound emission, free-bound emission, collisional cooling, heating through photoionization and heating from non-thermal electrons, determined by the Spencer-Fano routine’s last call in this cell. From these heating and cooling rates a net heating (or cooling) is constructed, and the  $T_{\text{cell}}$  is updated. The maximum  $dT_{\text{max}}$  per T\_SOLVER is set at 250 K times a damping factor (which is separate from the damping factor in the level population solver). Initially, the T-damping factor is 0.8 (and thus the

<sup>4</sup> This updated dampening scheme was found through trial runs to be a good balance for quickly converging both elements which prefer large dampening as well as elements which often require small dampening.

```

1 SUBROUTINE cell%NLTE_solver()
2   CALL self%T_solver()           ! Get a new T prior to main solver loop
3   DO WHILE (.NOT. self%T_converged) ! Until T converges (NLTE checks itself)
4     CALL set_heating(T_old)       ! Store heating terms from previous T_solver
5     CALL self%EXCION_solver()     ! Solve excitation, ionization structures of all elements in the cell
6     CALL self%T_solver()          ! Get new T
7     CALL set_heating(T_new)       ! Store heating terms from new T_solver
8     CALL update_T(T_old, T_new)   ! Also checks if self%T_converged should be flagged
9     IF (iteration == 150) self%T_converged = .TRUE.      ! After 150 iterations, stop NLTE_solving.
10 END SUBROUTINE cell%NLTE_solver
11
12 SUBROUTINE cell%EXCION_solver()
13   DO WHILE (.NOT. ALL(conv_el))    ! Until all elements are converged
14     IF (sf_flag) CALL SF(args)      ! Call Spencer-Fano subroutine to set non-thermal fractions
15     IF (.NOT. rt_flag) CALL self%OTS_PI() ! Use On-The-Spot PhotoIonization if no full RT present
16     DO iZ=1,len(self%active_Z_arr) ! For each element in the 'active elements array' in this cell
17       CALL get_atom(iZ, curAtom)    ! Turn iZ into the correct atomic data
18       CALL curAtom%make_matrix()   ! Create matrix with all rates between all levels
19       CALL curAtom%solve_pops()    ! Use jacobian to get new level populations
20       CALL curAtom%check_convergence(conv_el(iZ)) ! Check this element for convergence flag
21       IF (iteration == 200) conv_el(iZ) = .TRUE.      ! After 200 iterations per element, stop
22 END SUBROUTINE cell%EXCION_solver

```

**Figure 1.** A pseudo-code schematic for the NLTE\_SOLVER and the EXCION\_SOLVER subroutines. The EXCION\_SOLVER is responsible for determining the level populations of all elements present inside a cell, while the NLTE\_SOLVER combines this with finding the temperature  $T_{\text{cell}}$  through the T\_SOLVER.

maximum  $dT_{\text{max}}=200$  K). After 75 iterations of the NLTE\_SOLVER, this is reduced to 0.2, and after 110 iterations it drops to 0.02. The temperature update is constructed such that looping is avoided<sup>5</sup>.

Once the T\_SOLVER has finished, the NLTE\_SOLVER will check for the total convergence of the level populations and temperature. This is done by checking if the last step taken by T\_SOLVER is less than 0.1% of the current  $T_{\text{cell}}$  and if the ‘net heating rate’ is less than 5% of the total heating rate. The level populations themselves have previously been validated for convergence in the EXCION\_SOLVER, and thus are not checked here.

In van Baal et al. (2023) and van Baal et al. (2024), there were no non-local effects to consider for the cells, and as such once the NLTE\_SOLVER converged to a solution, the cell as a whole can be considered to have converged. Convergence failure is quite rare, but can occur, typically in cells with lower densities and with low energy deposition. Cells that fail to converge are excluded in the spectral synthesis.

### 2.3 Optically thin spectra

From the converged cells, optically thin emission packets are generated which are subsequently summed together for each viewing angle, accounting for the Doppler-shifted wavelengths and fluxes. In the optically thin limit, the only radiative transfer effect to consider is the local Sobolev escape probability  $\beta_S$  which is set by the optical depth  $\tau_S$  within this approximation:

$$\beta_S = \frac{1 - e^{-\tau_S}}{\tau_S}, \quad (1)$$

$$\tau_S = \frac{A_{ul}}{8\pi} \frac{g_u}{g_l} \lambda_{ul}^3 n_l \left(1 - \frac{g_l n_u}{g_u n_l}\right) t. \quad (2)$$

<sup>5</sup> In trials, it was noted that sometimes  $T_{\text{cell}}$  could loop between two values (e.g. 3100 K and 2900 K) until the damping factor reduced  $dT_{\text{max}}$ . If such a looping would occur, the new  $T_{\text{cell}}$  is set to 75% of the higher value plus 25% of the lower one.

Here, the subscripts  $u$  and  $l$  refer to the upper and lower state, respectively,  $A_{ul}$  is the transition strength from  $u$  to  $l$  with the corresponding wavelength  $\lambda_{ul}$  for this transition.  $g$  are the statistical weights,  $n$  the number densities, and  $t$  is the time.

The optically thin emission packets are generated by combining the Sobolev escape probability (Eq 1) with the transition probability, the energy difference between  $u$  and  $l$ , and the total amount of particles in the upper state,  $N_u$ , in that cell:

$$\text{Emission}_{ul}(\lambda) = A_{ul} \times \Delta E_{ul} \times \beta_{S,ul} \times N_u. \quad (3)$$

By combining the emissivity from every transition from every element in every cell together, the full optically thin spectrum can be constructed, if the Doppler-shift effects on the observer’s frame are accounted for to adjust the wavelength to the correct bin for the observer:  $\lambda_{\text{emit},ul}$  to  $\lambda_{\text{obs},ul}$ . A similar correction has to be made for correcting this emissivity<sub>ul</sub> into the observer’s frame. This completely optically thin emission is what was used in van Baal et al. (2023), and predominantly in van Baal et al. (2024), except for recombination emission with  $\lambda > 5000$  Å.

For recombination with  $\lambda \leq 5000$  Å, van Baal et al. (2024) instead applied an approximate ‘on-the-spot’ treatment for photoionization, as this effect mostly comes into play for blue wavelengths. The cut-off at 5000 Å was chosen as redder photons no longer had enough energy to do any photoionization, as only the ground state multiplet plus the next eight excited states were considered<sup>6</sup>. In the work presented here, we have improved slightly on the recombination emission calculations by including specific recombination rates for O I, Fe I and Fe II<sup>7</sup>. For the other elements, we follow the default treatment as in SUMO, allocating 1/3rd of the rate into the ground state and the rest distributed following statistical weights. Free-bound emission is

<sup>6</sup> Photoionization is much less effective at redder wavelengths, and as this approximation was only implemented in the emitting cell this limit had no significant impact on the total emission.

<sup>7</sup> With the total radiative recombination rates taken from [www.astronomy.ohio-state.edu/~nahar/nahar\\_radiativeatomicdata/index.html](http://www.astronomy.ohio-state.edu/~nahar/nahar_radiativeatomicdata/index.html), as in SUMO

only calculated from upper levels containing at least 4% of the total level population in that ion, using the following (see also Eq B.22 in [Jerkstrand et al. \(2012\)](#)):

$$j_{k,l}^{\text{f-b}} = \frac{1}{4\pi} n_e n_+ \alpha_{k,l}(T) * \left( 0.8kT + \chi_{k,l} \right), \quad (4)$$

which is emitted over a box-shaped profile between  $0.5 - 1.5 \text{ kT}$ .  $n_e$  is the free electron density,  $n_+$  is the number density of the ion,  $\alpha_{k,l}(T)$  is the specific recombination coefficient and  $\chi_{k,l}$  is the energy difference between the starting level and ionization threshold to reach this ion.

The cross section  $\sigma_{\text{PI}}$  due to this approximate treatment is calculated using the hydrogenic approximation ([Rybicki & Lightman 1979](#)) as follows (see also [Jerkstrand et al. 2012](#), appendix B6):

$$\sigma_{\text{PI}} = 7.9 \times 10^{-18} \times \left( \frac{\lambda_{\text{bin}}}{\lambda_{\text{ion}}} \right)^3 \times \frac{\left( 1 - \frac{E_u}{E_{\text{ion}}} \right)^{-0.5}}{(C_{\text{ion}} + 1)^2} \text{ cm}^2, \quad (5)$$

where  $\lambda_{\text{bin}}$  is the wavelength of the bin where the emission is emitted,  $\lambda_{\text{ion}}$  is the ionization threshold up to which a photon can ionize,  $E_u$  is the energy of the starting level,  $E_{\text{ion}}$  is the ionization threshold,  $C_{\text{ion}}$  is the charge of the starting level, and where the Gaunt factor has been assumed to be unity. The optical depth  $\tau_{\text{PI}}$  is then determined as follows:

$$\tau_{\text{OTS-PI}} = \sigma_{\text{PI}} \times n_u \times V_{\text{cell}}^{1/3}, \quad (6)$$

where  $n_u$  is the level population of this level, and  $V_{\text{cell}}$  is the volume of the cell where the recombination takes place. Taking  $V^{1/3}$  is a rough proxy for a length scale that the photons would travel in each cell, which might overestimate the absorption in the cell somewhat. However, since the approximation is only applied in the local cell, this partially evens out to some of this emission escaping to the next cell and being absorbed there which would happen in a non-local case. The absorbed emission is accounted for in the `T_SOLVER` as an additional heating source, and in the `NLTE_SOLVER` as photoionization.

All recombination emission is binned into bins with a width of  $50 \text{ \AA}$ . First all  $\tau_{\text{OTS-PI}}$  rates are calculated and then the actual rates are assigned depending on the relative contribution from each level, from each ion, to the total  $\Sigma \tau_{\text{OTS-PI}}$  within the bin where the emission took place. The binning is relatively rough, as the calculation of  $\sigma_{\text{PI}}$  is relatively expensive compared to the rest of the `NLTE_SOLVER`.

## 2.4 Radiative Transfer

In order to capture effects from the globally sourced radiation field, full radiative transport has to be implemented. In this work, we expand on the initial ‘on-the-spot’ photoionization treatment from [van Baal et al. \(2024\)](#) to compute the full transfer of radiation by considering photoionization and lines. The photoionization rates from [van Baal et al. \(2024\)](#) have been replaced by rates computed from the radiation field, and photoexcitation rates have been added.

The radiation field is both generated by the level populations in each cell, and interacts with them through photoionization and photoexcitation, so this mandates that `ExTrASS` should iterate between the `NLTE_SOLVER` and the new radiative transport module (`RAYTRACEGRID`). In Figure 2, a pseudo-code overview is given of this iterative process.

If no previous solution is loaded (line 2 in Figure 2), the `NLTE_SOLVER` will still use the ‘on-the-spot’ photoionization treatment from [van Baal et al. \(2024\)](#) in order to get an initial estimate for the photoionization rates, although photoexcitation is lacking in this

first solution. Subsequently, the emission from all cells is generated, by binning it by wavelength ( $400 - 25000 \text{ \AA}$ , with logarithmic step sizes of 0.1 %) to generate photon packets. Emission blueward of  $10000 \text{ \AA}$  is treated with the new radiative transport, while emission between  $10000 - 25000 \text{ \AA}$  is treated as before under the optically thin treatment<sup>8</sup>. The emission mechanisms considered are bound-bound emission, free-bound emission and two-photon emission for neutral H ([Nussbaumer & Schmutz 1984](#)) and He ([Li & McCray 1995](#)).

We use a ray-tracing technique to follow the path of the photon packets from their point of emission until they either escape the grid or less than  $10^{-6}$  of their starting energy remains. To limit memory usage of tracking the photoexcitation rates we adapt a domain decomposition scheme (see below) similar to [Brunner & Brantley \(2009\)](#), such that each node only stores rates for its own subdomain while still having an efficient global transport. Rays are emitted towards all viewing angles; we use  $20 \times 20$  viewers (as in [van Baal et al. 2023, 2024](#)) equally spread in the polar and azimuthal angles. The 400 beam directions give a satisfactory angular sampling to obtain good estimates for photoexcitation and photoionization rates in each cell.

The ray-tracing is done in a similar manner as described in [Jerkstrand et al. \(2020\)](#), their Sec 4.5), but with modifications to the optical depths and the division of emission into the energy packets ( $j_i$  in [Jerkstrand et al. 2020](#)). The first change is to calculate the optical depths with respect to photoionization, instead of Compton scattering, while the energy packet subdivision is altered to adjust for the solid angle of the viewing direction ( $\Delta\Omega_k$  in [Jerkstrand et al. 2020](#)). This is done because the viewing directions are not spread isotropically<sup>9</sup>, which means without such a correction the emission would not be isotropic as it should be. As a result, the final output spectra have to be re-corrected for this solid angle when checking for convergence<sup>10</sup>.

In each cell  $i$ , for each wavelength bin  $j$ , one ray will be sent towards each observer  $k$ ; thus the total number of rays can be computed ahead of time and used to verify when the radiative transfer has completed. Each ray has a number of photons  $N_{i,j,k}^{\text{phot}} = E_{i,j}^{\text{bin}} / \Delta\Omega_k / E_j^{\text{phot}}$ , where  $E_j^{\text{phot}}$  is the energy ( $hc/\lambda_j$ ) of an individual photon at the corresponding wavelength  $\lambda_j$  where the ray starts and  $E_{i,j}^{\text{bin}}$  is the starting emission in this bin and cell. The starting  $\lambda_j$  is chosen to correspond to the reddest  $\lambda$  of all features within the bin  $j$  (to avoid self-absorptions). Optical depths  $\tau_{\text{PI}}$  for photoionization are calculated and applied for every step the ray makes, which is either to the wall of the next cell or to a line (in the Sobolev approximation, line interactions happen at discrete resonance points). Photoionization calculations have been improved since [van Baal et al. \(2024\)](#) using data from [Verner et al. \(1996\)](#) for  $\sigma_{\text{PI}}$  from the ground state; excited states still use the hydrogenic approximation (see also Equation 5).  $\sigma_{\text{PI}}$  is only calculated for the ground multiplet plus the next 8 states<sup>11</sup>.

<sup>8</sup> This choice reduces the number of bins for which radiative transport is used to 3265, while it would be 4170 if the transport treatment was extended to  $25000 \text{ \AA}$ . As red wavelengths are less impacted by radiative transport effects, this gives a good compromise between computational costs and accuracy.

<sup>9</sup> With a setup of  $20 \times 20$  viewing angles for the polar $\times$ equatorial angles, viewing angles closer to the north/south poles are packed more tightly and cover a smaller patch of the sky.

<sup>10</sup> In [Jerkstrand et al. \(2020\)](#) the solid angle was omitted at both emission and escape time as only emergent ray intensities were of interest.

<sup>11</sup> Tests have shown that higher excited states have such low level populations that they do not significantly contribute to photoionization, and as such only these lowest energy levels are included for computational efficiency reasons, as the calculations of  $\sigma_{\text{PI}}$  are expensive.

```

1 CALL initialize%cells()           ! Prepare the grid with all data, and load previous solution if present
2 IF (.NOT. loaded_solution) CALL cell_arr%NLTE_solver() ! Run NLTE solver first if no previous solution
3 DO WHILE (.NOT. global_converged)
4   CALL reset_outputs()           ! Drop output from previous iteration
5   CALL cell_arr%prep_emission() ! Generate all the emission in all cells
6   CALL prepare_PIPE()           ! Initialize data structures for photoionization and photoexcitation
7   CALL RayTraceGrid()           ! Radiative Transfer module
8   CALL stitch_RTNLTE()          ! Connect RT data into NLTE module
9   CALL cell_arr%NLTE_solver()   ! Connect RT data into NLTE module
10  CALL check_convergence()      ! Check convergence and save NLTE data

```

**Figure 2.** A pseudo-code schematic for the full program flow of ExTraSS, and how the new RAYTRACEGRID interacts with the previous NLTE\_SOLVER. If there is no previous solution present, the NLTE\_SOLVER has to run first, to be able to generate the rays which are transported by the RAYTRACEGRID module.

If the ray hits a line (i.e.  $\lambda_{\text{ray}} = \lambda_{\text{line}}$ )<sup>12</sup>, the Sobolev optical depth  $\tau_{\text{line}}$  is used to attenuate  $N^{\text{phot}}$  by photoexcitation. Lines require a minimum optical depth of  $\tau_{\text{line}} > 10^{-3}$  to be used; lines below this limit are treated as optically thin and not stored. When rays escape the grid, their remaining energy is added to the spectrum of observer  $k$  at the Doppler-shifted wavelength for their starting cell  $i$  towards  $k$ . If the ray energy drops below  $10^{-6}$  of the starting value, the ray is considered destroyed. Electron scattering is currently not treated in the code, which means we do not capture the line peak blueshifting and red tail enhancement that can occur in early nebular phases.

Once the RAYTRACEGRID has finished, the photoionization and photoexcitation/photodeexcitation rates<sup>13</sup> are coupled back to the NLTE\_SOLVER to account for these rates in the next iteration. The global convergence is checked by comparing the total energy in the emergent spectra for all viewing angles (as well as any escaped emission further redwards of 25000 Å) to the total energy deposition inside the nebula, as the ratio between these should be close to unity when in the steady-state mode (the transfer introduces some adiabatic losses in a homologous flow, so the typical value is in the range of 0.9–1).

## 2.5 Jagged Arrays & shared memory

As simply storing the level populations across  $\sim 10^6$  cells, for 44 ions with a maximum of 100 excitation stages ( $N_{\text{lev}}$ ) each would already require  $\sim 4.4 \times 10^9$  numbers, which is  $\sim 35$  GB of RAM. Storing the photoexcitation rates would take another factor of  $N_{\text{lev}}$ ; this would clearly result in a problematic amount of data to hold in memory. As such, within ExTraSS a lot of care has been taken to design the code such that the memory usage has been optimized, through several means.

Firstly, critical components have been memory shared between cores on the same node, which limits how much RAM is taken up by a factor of  $N_{\text{cores-on-node}}$ , as such memory sharing can only be done for cores that are part of the same node. This includes – but is not limited to – large parts of the atomic dataset, the ‘basic’ cell data (e.g. where in the grid it is located, composition, temperature) and the output spectral data. For the output data, the final spectra are created by summing the spectra from the different nodes together, as each node holds only part of the total escaped emission.

The second step has been the implementation of “Jagged Arrays” in different places in the code. The main idea here is to only allocate

<sup>12</sup> Due to the redshifting of the ray in the co-moving frame, this occurs in the cell provided that  $\lambda_{\text{ray, start}}$  and  $\lambda_{\text{ray, exit}}$  straddle  $\lambda_{\text{line}}$ .

<sup>13</sup> With compensation for stimulated emission, see Appendix B.1 in Jerkstrand et al. (2012).

<i>A</i>	$n_1$	$n_2$	–	–	–	–	–	–	–
<i>B</i>	$n_1$	$n_2$	$n_3$	$n_4$	–	–	–	–	–
<i>C</i>	$n_1$	$n_2$	$n_3$	$n_4$	$n_5$	$n_6$	$n_7$	$n_8$	$n_9$
<i>D</i>	$n_1$	$n_2$	$n_3$	$n_4$	$n_5$	$n_6$	$n_7$	$n_8$	–
<i>E</i>	$n_1$	$n_2$	$n_3$	–	–	–	–	–	–
<i>F</i>	$n_1$	$n_2$	$n_3$	$n_4$	$n_5$	$n_6$	–	–	–

**Table 2.** A schematic overview of how Jagged arrays work within ExTraSS. Here a mock setup of 6 elements (*A* – *F*) which have a varying amount of excitation states to track is shown. With 6 elements with (at most) 9 excitation states, a rectangular matrix will allocate  $6 \times 9 = 54$  variables. By using Jagged arrays instead, only  $2 + 4 + 9 + 8 + 3 + 6 = 32$  variables are allocated. Places where – is used in the matrix indicate that there is no excited states for that element.

memory when it is needed – after all, not all 44 ions used within ExTraSS have (at least) 100 excitation stages, so for many species less data can be used. A small example of this is shown in Table 2, where the level populations of elements *A* through *F* can be stored in a normal, rectangular matrix (which would take 54 variables) or with a Jagged Array structure, using only 32 variables. This can be expanded to e.g. the photoexcitation rates, which would take 486 variables in the rectangular case, but only 210 in the Jagged Array setup.

Additionally, by storing the level populations of each ion as attachment to the cell, another redundancy can be avoided and we can directly store information for only the ions present in that cell. A cell with e.g. only elements *A*, *B* and *D* in a Jagged Array setup only takes 14 variables for the level populations, and 84 for the excitation stages.

Even with the combination of Jagged Arrays and shared memory, full 3D NLTE Radiative Transfer on large models will require a large amount of RAM. Further steps towards tractability requires a domain decomposition scheme which cuts the full problem into several smaller ones, and each node then only manages its assigned part. By only loading the part that the node is assigned to, the total memory usage on each node goes down and will scale proportional to how many nodes are being used – if the problem is too big, introducing more nodes will now reduce the memory requirements. Domain decomposition removes the roof on how detailed microphysics can be treated for a given problem set by node memory limits, opening the path towards highly accurate modelling.

## 2.6 Domain Decomposition

The domain decomposition scheme implemented in ExTraSS, to manage the memory load of 3D NLTE radiative transfer, is inspired by Brunner & Brantley (2009). The goal of this technique is to reduce memory load on the system at the cost of some communication

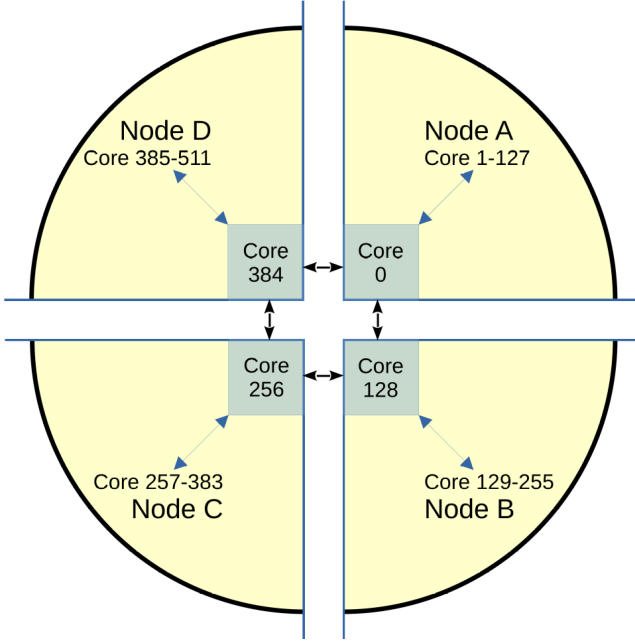


**Figure 3.** An equatorial slice of the 3D grid, to show how this is broken into four slices by the domain decomposition scheme, with the main communicating cores on each node marked, and the communication chains represented by the arrows. In this example, the nodes each have 128 cores, but this number will vary for different clusters.

overhead. This communication overhead can be reduced by properly splitting the full domain into smaller ones, which in our case means  $\phi$ -based decomposition, i.e. each node takes an equal part of the number of azimuthal slices to make a domain. Through (intra-node) memory sharing (Section 2.5), all critical information on the domain can be made available for each ray on that domain, further limiting memory usage.

The first component in a domain decomposition scheme is to set up the data communication between the different domains. In ExTraSS, this is done by having one core (the ‘manager’) on each node assigned to manage both the intra- and inter-node communication, while the rest of the cores generate and transport the rays. The manager cores talk both to each other (so cross-domain) to handle data transfer between the domains, as well as to all other cores on their node to assign incoming rays to new workers and to receive rays which need to be transferred to a different domain (bundles from emissivity are generated by workers themselves).

Transfer of data between cores on the same node is highly efficient and quick, while cross-node transfer is slower to initiate and should be done in fewer but more data-intensive steps. Optimization of bundle sizes for both types of transfer was done (see below), but it should be noted that differently sized grids and number of nodes will have different ideal sizes. In order to retain good scalability for the problem, communication is set up asynchronously, as this optimizes worker efficiency (Brunner & Brantley 2009).

In Figure 3, we schematically display the separation of a 2D circular grid (or, equivalently, an equatorial slice of a 3D spherical grid) into four domains, with each node receiving an equally sized slice. The arrows in Figure 3 outline the communication chains that are initialized alongside this domain-separation to perform the full transfer. Communication between nodes is performed exclusively by the manager cores, with any received data by them subsequently dis-

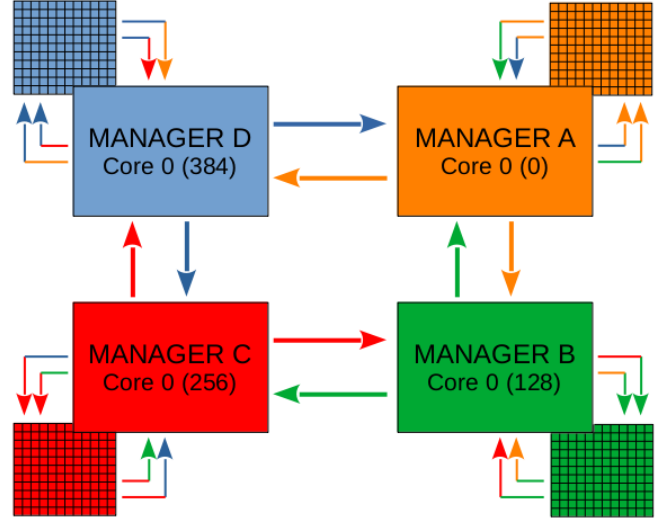


**Figure 4.** A schematic overview of all the communication streams for the four-domain setup from Figure 3. The grid of small blocks represents the 127 workers (cores 1-127 on each node) per node, the small arrows communication between each worker and their manager, and the bigger arrows between the different managers. Each node has its own colour, with the small arrows indicating both the ‘origin’ of the data (base) as well as the ‘target’ (head). Each arrow represents a different MPI communication stream – the small arrows represent all 127 streams between the workers and their manager.

tributed to the other cores on the node to perform the calculations. The number of used domains within ExTraSS is flexible; the representation with four slices is visually the cleanest while still outlining that only communication between neighbouring nodes is initialized.

A more detailed look at the communication chains initialized for the domain decomposition is shown in Figure 4. As shown by the amount of arrows, the data transfer between the managers is handled separately for the ‘up’ and ‘down’ streams. In Figure 5 we show pseudo-code for how the managers perform the MPI communication between both their own workers and to neighbouring managers, both for the ‘upstream’ case only for brevity (the ‘downstream’ case is equivalent).

We verified the robustness of the code both for the total number of domains used and for the size of the communication streams from the managers (both to other managers and to their own workers). For the current work, the domain decomposition is limited to only separating by  $\phi$ -angle (as is shown in Figure 3). The  $\phi$ -slicing is the simplest to implement, minimizes domain crossings and is optimal for maintaining (roughly) equal domain loads. As intra-node communication is more efficient, the data bundles between managers and workers are smaller than between managers on different nodes, hence the differently sized arrows to showcase this data bundle difference in Figure 4. As the worker-manager data bundles are smaller, there will be more of these bundles, also because every worker will have its own communication chain. The communication logic for the manager is shown in Figure 5; the ‘multiplier’ on line 11 corresponds to the size difference between the worker-to-manager data bundles and the manager-to-manager bundles.

The optimization of these bundle sizes depends quite strongly on the number of cores available on a node, the number of domains and to a lesser degree on the total number of rays that will be used in the radiative transfer. For the model shown here, nodes with 128 cores each were used, and the model was split into four domains as

Bundle Size	Multiplier	$t_{\text{last cell}}$ (s)	$t_{\text{term}}$ (s)	$\delta t$ (s)	Ranking $t_{\text{lc}} : t_{\text{term}}$
16384	18x	9057	9412	355	10 : 9
32768	12x	8159	8746	587	2 : 7
32768	24x	8252	8296	44	4 : 2
49152	24x	8284	8504	220	5 : 4
57344	24x	9034	9473	439	9 : 10
65536	20x	8294	8665	371	6 : 6
65536	22x	8133	8839	706	1 : 8
65536	24x	8241	8289	48	3 : 1
65536	26x	8351	8564	213	8 : 5
65536	30x	8309	8349	40	7 : 3

**Table 3.** Performance metrics, using  $3 \times 10^9$  rays across 20 000 cells with 512 cores across 4 nodes (the setup as shown in Figures 3 and 4), for worker-to-manager bundle size and node multiplier. The  $t_{\text{last cell}}$  indicates how quickly the program finished all cells, while the  $t_{\text{term}}$  indicates how long it took the program to finish up with all the packets that were still ‘stuck’ in the buffers at  $t_{\text{last cell}}$ . The time for this ‘flushing’ ( $\delta t$ ) is also listed. At different bundle sizes there are different optimal multipliers.

Run time (s/cell)	SF time (s/cell)	$t_{\text{best}}/t_{\text{worst}}$	Start	Pattern
457.3	430.9 (94.24%)	0.916	2 <sup>nd</sup>	always
103.6	77.5 (74.83%)	0.816	5 <sup>th</sup>	+10
110.0	84.1 (76.46%)	0.826	5 <sup>th</sup>	+7
112.5	87.4 (77.74%)	0.867	5 <sup>th</sup>	+5
122.5	96.6 (78.85%)	0.871	4 <sup>th</sup>	+10
135.9	108.8 (80.00%)	0.855	4 <sup>th</sup>	+7
133.6	108.0 (80.89%)	0.868	4 <sup>th</sup>	+5
141.0	114.9 (81.47%)	0.906	3 <sup>rd</sup>	+10
147.7	121.7 (82.40%)	0.828	3 <sup>rd</sup>	+7
158.6	131.9 (83.18%)	0.821	3 <sup>rd</sup>	+5
149.0	122.8 (82.42%)	0.810	2 <sup>nd</sup>	+10
161.4	134.7 (83.47%)	0.824	2 <sup>nd</sup>	+7
168.3	141.6 (84.12%)	0.770	2 <sup>nd</sup>	+5

**Table 4.** Run time outcomes for the NLTE\_SOLVER, depending on how often the Spencer-Fano subroutine is called, with the average times given per cell. The routine is always called on the first iteration, and then repeated from the ‘start’ iteration plus every ‘pattern’ iteration. The ratio between the quickest core to finish and the slowest core is also shown ( $t_{\text{best}}/t_{\text{worst}}$ ) – a ratio closer to 1 is more optimal. The time not spent in Spencer-Fano is approximately  $26 \pm 1$  s for all setups.

Figures 3 and 4 also indicate. For manager-to-worker communication, a bundle size of 65536 ( $= 2^{16}$ , ‘size’ on line 12 in Figure 5) was chosen, while manager-to-manager data bundles are 24 times larger, i.e. the manager cores can receive 24 data bundles from their workers before they initiate data transfer to the target node, and when they receive data from another manager they split this back down into 24 smaller bundles to hand back to their own workers (the ‘multiplier’ on line 11 in Figure 5). Several different sizes for both the worker-to-manager bundle size as well as the node multiplier were tested, with an overview given in Table 3.

As shown by the timing differences in Table 3, there is no monotonic relation between the bundle size and multiplier together. Generally, too small of a bundle leads to too much communication and this drags down the efficiency, while having too small of a multiplier instigates too many (smaller) communication streams between the different nodes. Several setup achieved very similar outcomes; however, a full 3D grid might send around a factor 100 more rays than used in the trial runs, and when more total rays are send, larger bundle sizes become preferred. As such, we opted for 65536 for the current setup, but this number is flexible. We tested several different node multipliers to accompany this bundle size, and settled on 24x as this was the fastest overall by a small margin, while also having one of the smallest  $\delta t$  ‘flushing’ times.

Due to the ray-tracing nature of our code, the total number of rays can be calculated before the radiative transfer begins, and this number is used to validate when the transfer has completed and all rays have either left the full grid, have been destroyed or are currently awaiting transfer to another domain. These last few rays are then handled before finalizing the radiative transfer and connecting the photoionization and photoexcitation data into the level population solver. The proper termination of these last few rays needs to be done carefully, to avoid the last rays from becoming ‘ignored’ or being ‘stuck’ while the code progresses to the next iteration of the NLTE\_solver. The transfer of these last rays has to be done in the correct order to avoid rays being missed, and must be sent even when the data buffers are not filled yet.

### 3 CODE VALIDATION

#### 3.1 NLTE solver setup

Compared to the 1D SUMO code, the level population solver part has been combined into one solver instead of separate excitation and ionization balances. This does mean that the matrix to solve for the level populations has to solve for all the ions within the atomic species at the same time, which increases the size of the matrix significantly. However, by limiting the number of excitation states used to 100 per ion, the total size of the matrix is reduced to  $300 \times 300$ , which is smaller than the excitation matrix for the largest ions in SUMO. As such, within ExTrASS the largest computational component within the NLTE\_SOLVER is the Spencer-Fano routine, especially after the inclusion of the excitation channel in this work.

As a result, the Spencer-Fano calls are made with some restriction. Testing (on the model from van Baal et al., submitted) indicated that only very small differences were found in the outcome ( $T$  and the free electron fraction  $x_e$ ) of the level population solver, even when Spencer-Fano was called much more often. In Table 4 we showcase several settings for how often Spencer-Fano was called, by having each core compute six representative cells from initialization until the NLTE\_SOLVER converged (including the ‘on-the-spot’ local photoionization treatment, and no non-local transfer effects). Usually, within the global iterative scheme, the NLTE\_SOLVER will become quicker to run at later iterations as most cells quickly converge, while the radiation transport still requires the same amount of rays to be computed, and as such the first, pre-radiative transfer iteration of the NLTE\_SOLVER is the most computationally expensive one.

As shown in Table 4, if we recompute the non-thermal energy distribution with Spencer-Fano every iteration, almost 95 % of the total time in the NLTE\_SOLVER is spent on that subroutine alone, and it takes approximately 7.5 minutes on average per cell. By only recomputing occasionally, a lot of time can be saved, although the exact pattern for this recomputing has a strong impact. Recomputing starting on the second iteration leads to relatively poor balance be-

```

1 DO WHILE (.NOT. RT_finished)           ! Until global termination signal
2   DO w = 1, nr_of_workers             ! Check all workers 'w' for worker-to-manger incoming data
3     CALL upstream_worker(w, upsend_Node) ! Check if worker has data to pass 'upstream'
4     IF (upstream_Node) CALL MPI_ISEND(upsend_Node) ! If data bundle to 'UP' is full, non-blocking SEND
5   ENDDO
6   CALL MPI_TEST(upreceive_Node, upN_flag) ! Check if the 'UP' side has given data
7   IF (upN_flag) THEN
8     local_buffer = upreceive_Node      ! Copy data
9     CALL MPI_IRecv(upreceive_Node)     ! Ask for new data in non-blocking manner after data was copied
10    DO i = 1, multiplier             ! For the size difference in MtW / MtM data bundles
11      CALL find_recv_worker(workID)   ! Look for available worker (workID)
12      CALL MPI_ISEND(local_buffer((i-1)*size:i*size), workID)
13    ENDDO
14  ENDIF
15 ENDDO

```

**Figure 5.** A pseudo-code schematic of how the non-blocking MPI communication is implemented. This shows the communication steps taken by the manager towards the workers on the same node (lines 2-5), as well as cross-node to other managers (lines 6-14). The same logic is used for the “downstream” side. The data received from another node is copied to a local buffer, such that the non-blocking IRecv request to the other manager can be made immediately.



**Figure 6.** A look at the FPE and activity threads during one full iteration of RAYTRACEGRID (highlighted region). The green region (80 %) corresponds to main thread computations, while the blue corresponds to MPI (20 %). The MPI starts picking up when the first cores complete the ray tracing of all rays that they generate themselves, at which point they start checking for incoming data onto their domain through MPI calls. The median FPE sits around 35 % for the first half of the module, and then peaks at over 60 % just before MPI comes in, with the FPE dropping as more and more cores start their MPI calls.

tween the quickest and slowest cores ( $t_{\text{best}}/t_{\text{worst}}$  drops to  $\sim 0.8$  for these setups). The load balance is quite important to optimize as it makes the code much more predictable in run times when using more or fewer cores. Because of this, the setups where the recomputing begins on iteration 4 are quite attractive – although they have worse load balancing than when computing every iteration, all three setups have quite similar  $t_{\text{best}}/t_{\text{worst}}$ . This highlights that recomputing by iteration 4 is quite important for convergence stability, which is why the setup of 4<sup>th</sup>+10 was chosen despite it not being the fastest overall.

### 3.2 Radiative Transfer setup

ExTraSS employs a ray-tracing setup for its radiative transfer module, rather than a Monte Carlo setup (which is used for the  $\gamma$ -ray transport). By using a ray-tracing setup, we ensure that every energy bin from every cell is given a chance to create a non-local radiation field impact towards all viewing angles, while also minimizing the total number of photon packets used per iteration of the RAYTRACEGRID module. If a Monte Carlo setup had been used to choose the initial direction of each photon packet, we would have to use many more packets to ensure that the emission is done isotropically. A Monte Carlo setup would have the benefit of being able to treat scatterings (due to e.g. dust or electrons) more naturally than in the ray-tracing setup. However, in the current version of ExTraSS, these effects are not included.

As shown in Figure 2, there are several ‘translation’ steps between the NLTE\_SOLVER and the RAYTRACEGRID modules. In terms of run time, none of these take a substantial amount of time, although specifically lines 5 and 6 together use more RAM than any other part of the code as they initialize all the emission features, and then trim down to select the features with  $\tau_{\text{line}} > 10^{-3}$  to store them for photo-

toexcitation calculations. The emission features are also combined into the emission bins which are used to send off all the rays.

As the memory limits are set outside of RAYTRACEGRID itself, the main validation here then is to check that the module runs efficiently and converges on sensible outputs. Unlike the NLTE\_SOLVER, there is not one main component within the RAYTRACEGRID module which will dominate the run times, and instead several components each have to be carefully designed to optimize the run times of the whole module.

When validating our results from the radiative transport, we compare against the data from Jerkstrand et al. (2018), who computed a 1D version of the s9.0 model, the 3D version of which is analysed in detail in van Baal et al., submitted. This gives us the most direct handle to compare photoionization and photoexcitation rates and level population distributions between the two codes to confirm that ExTraSS converges correctly.

#### 3.2.1 Efficiency

A good measure for the efficiency between the different calculations performed in RAYTRACEGRID is that no single part takes up a dominant amount of the run time, as well as having a good CPU floating-point efficiency (FPE) throughout the run. Over the whole RAYTRACEGRID module, the median FPE sits at just under 40 %, but this fluctuates depending on how far into the ray tracing the module is.

The rays are emitted from the inner cells first, which are smaller, denser, and need to undergo more cell crossings before they can (potentially) escape the grid. As such, for these inner cells, relatively more time is spent in determining the next location (edge of the cell, or the point where  $\lambda_{\text{ray}} = \lambda_{\text{line}}$  if a line is hit), rather than updating

to the new location and calculating the photoionization losses. As the cores get towards calculating the rays which originate further out into the nebula, instead the focus shifts into calculating these cross sections and location updates, which improves the FPE, as can be seen in Figure 6.

As not all cores will finish the ray tracing of their generated rays at the same time, towards the end of the module more time is spent in the MPI communication chain, where the workers begin checking with their manager if there is new data that has entered their node and that needs to be computed (the manager version of this communication is shown in Figure 5). As MPI calls are not particularly efficient in terms of FPE, this drags down the median towards the end of the RAYTRACEGRID. Figure 6 also shows that the timing difference  $t_{\text{best}}/t_{\text{worst}} \approx 0.7$ , for when the cores complete the ray tracing of their own generated rays. However, having a few cores finish relatively fast on each node can be beneficial for the overall run time of the program, as these cores will then take priority for calculating rays that have entered their domain, while other cores on their domain are still busy calculating their own assigned rays.

The primary computational bottlenecks in the RAYTRACEGRID module are the cross sections for photoionization, followed relatively distantly by the calculation to determine which cell wall is hit (that calculation is explained in detail in the Appendix of Jerkstrand et al. 2020). Towards the end of the module, when most cores have finished their assigned rays, a relatively large chunk of time is lost to MPI communication as there are more workers asking for new rays than new incoming rays.

### 3.2.2 Photoionization

In Figure 7 the position angle-averaged photoionization rates in ExTraSS for the  $9.0 M_{\odot}$  3D model (solid lines) are compared against the 1D rates from Jerkstrand et al. (2018) which were computed with SUMO (dashed lines). The rates shown for ExTraSS are the median rates at each velocity. The rates are shown for Ca I (which has the lowest ionization threshold of all used atomic species, at 6.113 eV), Fe I (which is the first species not predominantly ionized, ordered by ionization threshold) and O I (the hardest species to ionize which has nebular phase emission in the optical range)<sup>14</sup>.

It can be seen that for Ca I (green), the rates in ExTraSS are roughly one order of magnitude higher for most of the ejecta, and are high enough to fully ionize Ca I  $\rightarrow$  Ca II (i.e., leave only trace amounts of Ca I) throughout the ejecta. For Fe I, the rates are somewhat lower in ExTraSS although there is a bump around  $\sim 300 \text{ km s}^{-1}$ , and at the outermost ejecta ( $\gtrsim 1000 \text{ km s}^{-1}$ ) the rates are very similar. For O I, the rates in ExTraSS are significantly lower in the innermost ejecta where SUMO has very limited O (see Jerkstrand et al. 2018, Figure 2,  $^{56}\text{Ni}$  zone) while in ExTraSS the composition in this region holds a few percent oxygen. From  $\sim 500 \text{ km s}^{-1}$  outwards the rates are quite similar, with ExTraSS eventually achieving higher rates than in SUMO. Generally, these results show that the photoionization rates calculated with ExTraSS are in the right ball-park and comparable to similar, 1D codes.

<sup>14</sup> Ar and Ne have no optical nebular phase lines, and He only has a very weak feature at He I  $\lambda 7065$  which is barely above noise levels, for the model used.

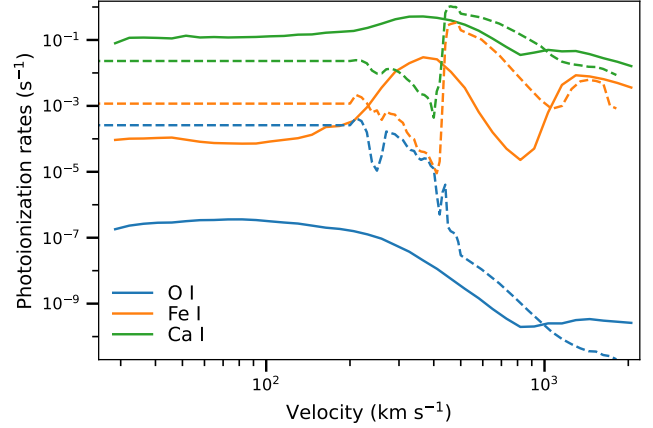


**Figure 7.** Comparison of the 3D photoionization rates from ExTraSS for the s9.0 model, in solid lines, against the rates in the 1D model from Jerkstrand et al. (2018), dashed lines, for oxygen (blue), iron (orange) and calcium (green). The decrease in the photoionization rate for Fe I around  $800 \text{ km s}^{-1}$  does lead to a corresponding rise in the neutral Fe fraction.

### 3.2.3 Photoexcitation

In Figure 8 the position angle-averaged photoexcitation rates in ExTraSS for the  $9.0 M_{\odot}$  3D model (solid lines) are compared against the 1D rates from Jerkstrand et al. (2018) which were computed with SUMO (dashed lines). The rates shown for ExTraSS are the median rates at each velocity. The rates are shown, from top to bottom, for H $\alpha$  (transition  $2 \rightarrow 5$ , which is the bluest component in H $\alpha$ ), Ca II  $\lambda 8498$  (the blue line in the NIR triplet), Fe I  $\lambda 5060$  (the first allowed transition to the ground state in neutral Fe) and [O I]  $\lambda\lambda 6300, 6364$  (the blue component of the [O I]  $\lambda\lambda 6300, 6364$  doublet).

These lines were chosen as they span a large range of photoexcitation rates for a series of relevant transitions (H $\alpha$ , Ca II  $\lambda 8498$  and [O I]  $\lambda 6300$ ) or because they concern a low-lying allowed transition to the ground state for an element that is present throughout the entire ejecta (Fe I  $\lambda 5060$ ). Although O and H are present throughout the ejecta in the 3D model for ExTraSS, they are only present outside of the  $^{56}\text{Ni}$  core in the 1D model, and hence they only appear at  $v \gtrsim 350 \text{ km s}^{-1}$ . For Fe and Ca, although these elements are present at these low velocities in 1D, this inner region contains very little mass and is modelled in a relatively large velocity step.

It can be seen in Figure 8 that ExTraSS and SUMO largely find similar photoexcitation rates for the different elements throughout the ejecta, across a large range of photoexcitation rates. For H $\alpha$ , the initial rate in SUMO is much higher, but in these velocity ranges there is very little H present in the 1D model, and as such this discrepancy is not of major concern. Past  $v = 400 \text{ km s}^{-1}$ , the median rate in ExTraSS is in very good agreement to the rates in SUMO.

For Ca II  $\lambda 8498$ , the agreement in the photoexcitation rates is even better. In the 1D core region ( $200 \leq v \leq 450 \text{ km s}^{-1}$ ) the rate fluctuates a bit, but generally similar rates are found with ExTraSS at this velocity range. For the outermost zones in 1D, the optical depth for this Ca II feature is too low (the cut off in SUMO is  $\tau_{\text{line}} \leq 10^{-2}$ , while it is  $\tau_{\text{line}} \leq 10^{-3}$  in ExTraSS) and thus there is no rate to compare at the highest velocities, but the rate in 3D remains compatible with the rates in 1D at their highest velocity.

Fe I  $\lambda 5060$  is largely similar to Ca II, but at rates approximately 100x lower. The match between 1D and 3D is quite good, except perhaps for the outer core region where 1D is a bit lower than 3D.

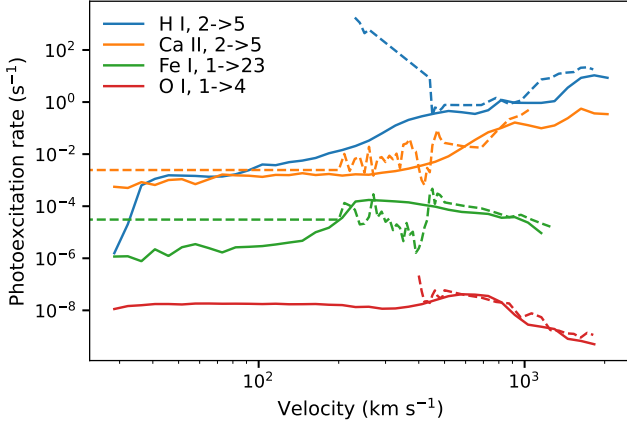


**Figure 8.** Comparison of the median 3D photoexcitation rates from ExTraSS (solid lines), against the rates from SUMO, using the 1D model from Jerkstrand et al. (2018) (dashed lines), for a series of elements.  $H\alpha$  is shown in blue, Ca II  $\lambda 18498$  in orange, Fe I  $\lambda 5060$  in green and [O I]  $\lambda 6300$  in red.

Also for this Fe I line, at the highest velocities the optical depth is too low to be considered, but now also in 3D this line is not accounted for any more, which indicates that the optical depths between the two models are also reasonably in agreement. It should be noted that the Fe I line is not present in every cell in 3D, and in particular at  $350 - 500 \text{ km s}^{-1}$ , where the largest difference to 1D is found, the line is only present in around 1/4th of the cells with these velocities. At every other velocity (up to  $1000 \text{ km s}^{-1}$ ) the line is present in at least half the cells.

For [O I]  $\lambda 6300$ , the photoexcitation rates match very well past  $400 \text{ km s}^{-1}$ , as that is where O is present in the 1D model. The rate in 3D is very flat for the inner region, even more so than the Ca II line was. Unlike the other lines, the photoexcitation rate for [O I] actually decreases above  $1000 \text{ km s}^{-1}$  by roughly an order of magnitude, but this occurs in both 1D and 3D.

### 3.2.4 Level Populations

In Figure 9 we look at the level populations of the first 100 levels Fe I (as we do not include more in ExTraSS) and compare the median values per radius in ExTraSS (right panels) to the level populations in SUMO (left panels). The relative fractions (bottom panels) show that there is quite good agreement between the ExTraSS populations and SUMO – the higher lying levels have somewhat higher populations, but this can be attributed to the higher densities in the 3D model ran with ExTraSS, which mean that these levels are a bit more populated. In particular for the darker colours (lower radii), the agreement is good between the two codes. The usage of a sharp cutoff of only 13 photoionization levels (Fe I has a ground state multiplet of 5 plus an additional 8 are used) can also clearly be seen in the ExTraSS level populations and their fractions.

Neutral iron is an important ion to investigate level population wise, as it retains relatively high population fractions for states past the first few multiplets. For many other important species (e.g. neutral hydrogen, carbon and oxygen), only the first 5–10 levels hold a significant fraction of the total level population. Emission wise, Ca II is also an important species to check if SUMO and ExTraSS have similar level populations, as it is responsible for both the [Ca II]  $\lambda\lambda 7291, 7323$  forbidden doublet and the Ca II  $\lambda\lambda\lambda 8498, 8542, 8662$  near-infrared triplet. In Figure 10, this comparison is shown. It can be seen that in

both codes, past the first few states the level populations drop drastically, although there are a series of levels (e.g. 20, 21, 41–45) where the populations are somewhat higher. This is because for these levels, our atomic data has no bound-bound transitions to lower states, so these states do not depopulate as strongly as the others which have several allowed bound-bound transitions. SUMO shows a somewhat larger drop from high density to low density (dark colours correspond to inner radii, where the density is higher) than the median ExTraSS values, but overall there is good agreement on the level population spread for Ca II.

## 4 DISCUSSION

### 4.1 Alternative Radiative Transfer schemes

Several alternative options exist when choosing how to perform the radiative transfer scheme as implemented in ExTraSS. Our chosen scheme, as outlined above, has one core per node (the manager) dedicated to manage all the communication for the photon packets leaving the domain and for the packets entering, and distributing these incoming packets to the other cores (the workers). This choice is particularly efficient for systems with a large amount of cores per node (CPN), as it only sacrifices  $1/N_{\text{CPN}}$  to the communication chain. Perhaps systems exists where each node has such a high CPN that one manager alone cannot manage all the communication without significant ‘buffering’ for the workers, but even with 128 CPN this does not occur. The risk of buffering is also reduced by giving the workers a secondary memory chunk to use while they are waiting for their previous communication to be confirmed to be completed; unless this second buffer is filled with data before the first communication completes, the worker can keep on calculating and will not buffer.

An alternative strategy which can be considered instead of the manager-worker setup, is to ‘link’ the cores on each node to one specific partner on their neighbour nodes. This simplifies the MPI communication chain significantly, since now the workers will directly transfer photon packets between themselves, rather than passing it to a manager, who gives it to another manager, and then back down to a worker. This link can easily be established using e.g. the internal rank that each core has on their node, and matching the cores with the same internal ranks. Using Figure 3 as example, core 1 on Node A would link to Core 129 on Node B, and Core 385 on Node D, as each is ‘rank-1’ on their own node. However, despite the simplified communication setup, there is significant risk with this setup that a large fraction of all cores will idle towards the end of the radiative transport calculations, if one specific set of linked cores would take much longer. This setup has no immediate way to offload incoming photon packets to already-completed cores, and if such an offloading mechanism were to be implemented, it will mandate more MPI communication which this setup was trying to simplify. For systems with a low CPN, this might still be a decent approach, but with more cores the risk in load-imbalances becomes much larger.

Another option which was considered for the radiative transport was to make use of shared memory for the entire setup, and have the cores ‘scan’ through all the cells within their domain. Each cell has an assigned ‘calculator’ for the NLTE\_SOLVER, and that core has access to the level populations within that cell, and thus would be able to calculate the radiative transfer effects. When the photon packet is moved to the next cell, the ‘current cell’ of the packet would be updated, and then the core which is the calculator for that cell will eventually update that packet through the new cell. This

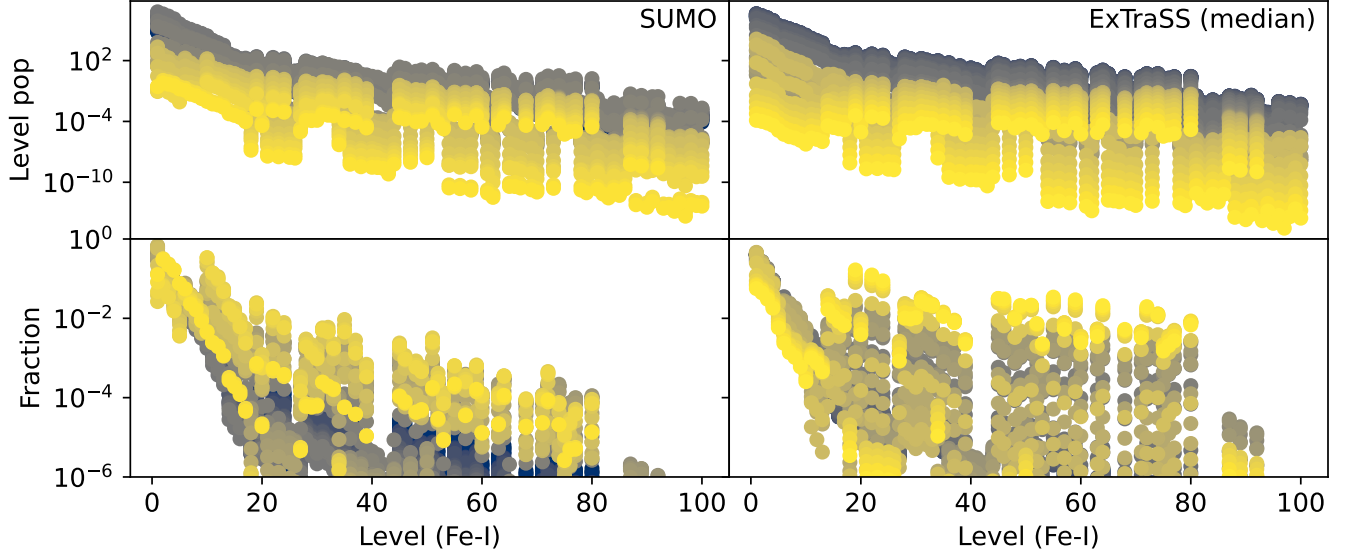


**Figure 9.** Comparison of the median Fe I level populations from ExTraSS for the s9.0 model (exploded by Stockinger et al. 2020, see van Baal et al., submitted for a detailed nebular phase analysis), against the rates in the 1D model from Jerkstrand et al. (2018) in the top panel, and the relative fractions of the levels in the bottom panel. Lighter colours correspond to radii with higher velocities. For both ExTraSS and SUMO, all radii are shown (median values for ExTraSS).

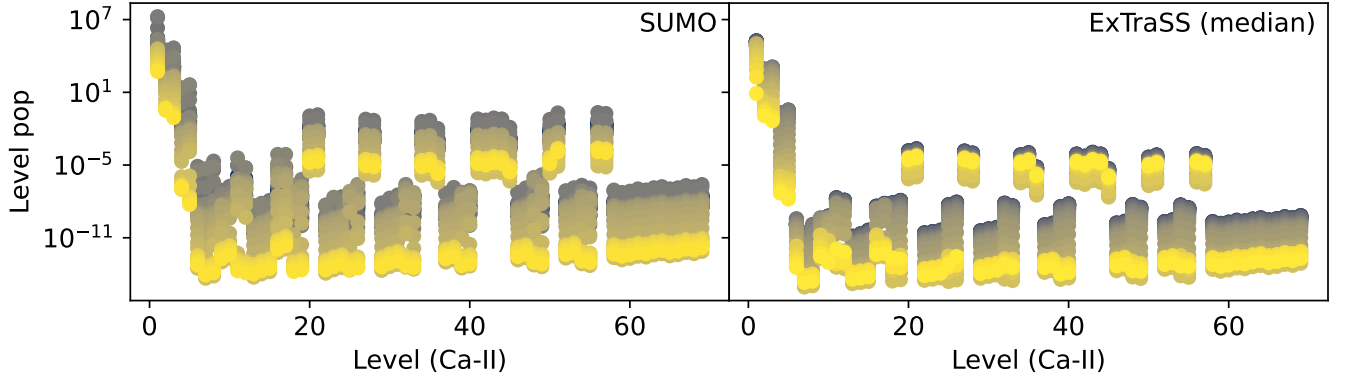


**Figure 10.** The same as in Figure 9, for for Ca II instead. As the fractions drop below  $10^{-5}$  past level 5, the fraction panels are not shown here for clarity.

setup would completely eliminate the intra-node communication (as the packets can be accessed through shared memory), and would be able to do cross-node transfers with minimal communication as well, as one core on each node can be assigned to also take care of the communication (which only comes with a minor cost, as it is a direct, single-step exchange without further 'distribution' to other workers). This setup would have a very minimalistic MPI communication setup, but comes with significant concerns regarding efficiency both in load-balance and shared-memory delays. It is unclear if having a large array of shared photon packets would cause delays due to accessing the shared memory by itself, and also for load-balancing here the issue remains that if one core, or even one domain, takes significantly longer than the rest, the total efficiency will drop significantly.

Between the three considered options for the radiative transfer, the chosen scheme has the most complex MPI communication setup, as it requires a chain of 'worker-to-manager-to-manager-to-worker' to transfer a photon packet from one domain to another. Of course, this is not done for each individual photon, but rather for a whole

bundle of them together, which does improve the efficiency of the communication chain significantly. The 'linking' strategy would have a much more straight-forward MPI communication chain, but will most likely not reach good load balance, and thus fall off in efficiency towards the end of the RAYTRACEGRID module. In Figure 6, it can be seen that as more and more cores finish with their own packets in the chosen setup, the CPU floating point percentage drops; such an effect would be even more severe for the 'linking' strategy as there is never any new work to do for a linked set of cores once they complete their own packets, while in the chosen setup the finished cores can pick up some transferred bundles. The third setup eliminates MPI communication almost completely through the power of shared memory, but has even worse load balancing issues looming and it is unclear if the shared memory access for the photon array can keep up with the efficiency of MPI communication, which might also slow it down.

## 4.2 Future code updates and applications

In its current form, ExTraSS is set up as a domain decomposed 3D NLTE radiative transfer code, which accounts for both photoionization and photoexcitation using the Sobolev formalism. It currently does not treat either electron scattering, dust or molecules; each could conceivably have impacts at various epochs in the nebular phase. Electron scattering would be important for earlier times, when densities are somewhat higher (see also [Jerkstrand 2017](#)). Dust tends to be more important at later times, as the ejecta cool and dust as well as molecules can begin to form.

Molecules are a complex topic within nebular phase SNe. They can form quite early (e.g. carbon monoxide was detected 112 days after explosion in SN 1987A, [Oliva et al. 1987](#), [Spyromilio et al. 1988](#)) but can also become depleted onto dust over time ([Wooden et al. 1993](#)). Molecules have been detected in old remnants (e.g. Cas A, [Rho et al. 2024](#)), as well as at early times, such as recently in the nearby hydrogen-rich SN 2023ixf ([Park et al. 2025](#)) as well as a few months after explosion for the Type Ic SN 2020oi ([Rho et al. 2021](#)). Efforts to include molecules for spectral modelling are so far limited to 1-zone or 1D modelling ([Liu & Dalgarno 1995](#); [Liljegren et al. 2020, 2023](#); [McLeod et al. 2024](#)).

Other improvements aside from the ones mentioned above, which can be made for ExTraSS in the future, are to account for time dependence, to add additional processes to the rate equations (e.g. charge transfer and collisional ionization, which are not yet treated), or to include free-free absorption in the radiative transfer. Models which have been used so far ([van Baal et al. 2023, 2024, submitted](#)) have not included odd-Z elements (e.g. N, Na) many of which are known to have non-negligible emission in the optical range, and these could be included in the future by correcting for the solar abundance ratio, for example. Other approximations include to only model up to 100 excitation stages per ion species, which could be relaxed for key ions in future work, and adiabatic expansion and cooling effects are not included. As ExTraSS assumes homologous expansion, the  $^{56}\text{Ni}$ -bubble effect ([Gabler et al. 2021](#)) can be accounted for in the hydrodynamical modelling of the input models, but not in the homologous ‘fast-forwarding’ afterwards.

## 5 CONCLUSIONS

In this work, we present ExTraSS (EXplosive TRAnsient Spectral Synthesis) – a 3D NLTE radiative transfer code for supernovae. The code has been upgraded to include photoionization and photoexcitation rates computed from the global radiation field, using a domain decomposition approach which enables the detailed micro-physics needed for NLTE modelling also in 3D.

As a result of the addition of radiative transfer, ExTraSS now iterates between solving for levels populations, temperature, and radiation field. Here we describe how we optimized both the level population solver and the radiative transfer module. The level population solver now also includes non-thermal excitations (in addition to ionizations) from the Spencer-Fano calculation ([Spencer & Fano 1954](#); [Kozma & Fransson 1992](#)), which mandated an adjustment to the solver to optimize the run time. The radiative transfer module required the introduction of domain decomposition due to memory limitations, and our choices surrounding the design of this are discussed.

The results of the new radiative transfer module are compared to the 1D s9.0 model analysed with SUMO by [Jerkstrand et al. \(2018\)](#), as this is the same input star as for the work in [van Baal et al., submitted](#),

except it was a 1D model rather than a 3D model as in the new work. The rates for photoionization across several species is shown to be compatible between ExTraSS and SUMO, while photoexcitation rates between the two models are in excellent agreement. Some variation exists in the exact level populations between the two codes, but this can be plausibly explained by the different structures (the 3D model is denser at the same epoch) and code setups.

With the upgrade presented in this work, ExTraSS has been established as a domain decomposed, 3D NLTE radiative transfer spectral synthesis code aimed at the nebular phase. It currently has only been applied to core collapse supernova models at late times, but in the future the code can be used for a wide variety of input models and different explosive transient mechanisms, if certain additional physical components are included. Such expansions will be outlined in future works, but in its current form, ExTraSS can be applied to a large set of SN models, to study their spectral signatures, and better constrain explosion properties, ejecta masses, and composition.

## ACKNOWLEDGEMENTS

The authors acknowledge support from the European Research Council (ERC) under the European Union’s Horizon 2020 Research and Innovation Programme (ERC Starting Grant No. [803189], PI: Jerkstrand) and the Knut and Alice Wallenberg Foundation (Project “Gravity Meets Light”, PI: Rosswog and Jerkstrand). The computations were enabled by resources provided by the National Academic Infrastructure for Supercomputing in Sweden (NAIIS) at the PDC Center for High Performance Computing, KTH Royal Institute of Technology, partially funded by the Swedish Research Council through grant agreement no. 2018-05973.

## DATA AVAILABILITY

The Data underlying this article will be shared on reasonable request to the corresponding author.

## REFERENCES

- Alme H. J., Rodrigue G. H., Zimmerman G. B., 2001, *The Journal of Supercomputing*, 18, 5
- Alp D., Larsson J., Fransson C., Gabler M., Wongwathanarat A., Janka H.-T., 2018, *ApJ*, 864, 175
- Axelrod T. S., 1980, PhD thesis, University of California, Santa Cruz
- Barmentlo S., Jerkstrand A., Iwamoto K., Hachisu I., Nomoto K., Sollerman J., Woosley S., 2024, *MNRAS*, 533, 1251
- Baron E., et al., 1995, *ApJ*, 441, 170
- Blondin S., et al., 2022, *A&A*, 668, A163
- Botyánszki J., Kasen D., Plewa T., 2018, *ApJ*, 852, L6
- Branch D., 1980, in Meyerott R., Gillespie H. G., eds, American Institute of Physics Conference Series Vol. 63, Supernovae Spectra. AIP, pp 39–48, doi:10.1063/1.32213
- Brunner T. A., Brantley P. S., 2009, *Journal of Computational Physics*, 228, 3882
- Dessart L., Hillier D. J., Sukhbold T., Woosley S. E., Janka H. T., 2021, *A&A*, 656, A61
- Filippenko A. V., 1997, *ARA&A*, 35, 309
- Fransson C., Chevalier R. A., 1989, *ApJ*, 343, 323
- Gabler M., Wongwathanarat A., Janka H.-T., 2021, *MNRAS*, 502, 3264
- Gal-Yam A., 2017, in Alsabti A. W., Murdin P., eds, , *Handbook of Supernovae*. p. 195, doi:10.1007/978-3-319-21846-5\_35
- Heger A., Fryer C. L., Woosley S. E., Langer N., Hartmann D. H., 2003, *ApJ*, 591, 288

Hillebrandt W., Kromer M., Röpke F. K., Ruiter A. J., 2013, *Frontiers of Physics*, **8**, 116

Hillier D. J., Dessart L., 2012, *MNRAS*, **424**, 252

Hoeflich P., Khokhlov A., 1996, *ApJ*, **457**, 500

Jerkstrand A., 2017, in Alsabti A. W., Murdin P., eds, , Handbook of Supernovae. p. 795, doi:10.1007/978-3-319-21846-5\_29

Jerkstrand A., 2025, *Living Reviews in Computational Astrophysics*, **11**, 1

Jerkstrand A., Fransson C., Kozma C., 2011, *A&A*, **530**, A45

Jerkstrand A., Fransson C., Maguire K., Smartt S., Egon M., Spyromilio J., 2012, *A&A*, **546**, A28

Jerkstrand A., Ertl T., Janka H. T., Müller E., Sukhbold T., Woosley S. E., 2018, *MNRAS*, **475**, 277

Jerkstrand A., et al., 2020, *MNRAS*, **494**, 2471

Jerkstrand A., Milisavljevic D., Müller B., 2026, in Encyclopedia of Astrophysics. pp 639–668, doi:10.1016/B978-0-443-21439-4.00090-0

Kasen D., Thomas R. C., Nugent P., 2006, *ApJ*, **651**, 366

Kerzendorf W. E., Sim S. A., 2014, *MNRAS*, **440**, 387

Kozma C., Fransson C., 1992, *ApJ*, **390**, 602

Kozma C., Fransson C., 1998, *ApJ*, **496**, 946

Kromer M., Sim S. A., 2009, *MNRAS*, **398**, 1809

Li H., McCray R., 1995, *ApJ*, **441**, 821

Liljegegren S., Jerkstrand A., Grumer J., 2020, *A&A*, **642**, A135

Liljegegren S., Jerkstrand A., Barklem P. S., Nyman G., Brady R., Yurchenko S. N., 2023, *A&A*, **674**, A184

Liu W., Dalgarno A., 1995, *ApJ*, **454**, 472

Lucy L. B., 2005, *A&A*, **429**, 19

Maeda K., Nomoto K., Mazzali P. A., Deng J., 2006, *ApJ*, **640**, 854

Mazzali P. A., Lucy L. B., 1993, *A&A*, **279**, 447

Mazzali P. A., Nomoto K., Patat F., Maeda K., 2001, *ApJ*, **559**, 1047

McLeod C., Hillier D. J., Dessart L., 2024, *MNRAS*, **532**, 549

Nussbaumer H., Schmutz W., 1984, *A&A*, **138**, 495

Oliva E., Moorwood A. F. M., Danziger I. J., 1987, *The Messenger*, **50**, 18

Park S. H., et al., 2025, *arXiv e-prints*, p. arXiv:2507.11877

Rho J., et al., 2021, *ApJ*, **908**, 232

Rho J., et al., 2024, *ApJ*, **969**, L9

Rybicki G. B., Lightman A. P., 1979, Radiative processes in astrophysics

Shingles L. J., et al., 2020, *MNRAS*, **492**, 2029

Siegel A., Smith K., Fischer P., Mahadevan V., 2012, *Journal of Computational Physics*, **231**, 3119

Spencer L. V., Fano U., 1954, *Physical Review*, **93**, 1172

Spyromilio J., Meikle W. P. S., Learner R. C. M., Allen D. A., 1988, *Nature*, **334**, 327

Stockinger G., et al., 2020, *MNRAS*, **496**, 2039

Taubenberger S., 2017, in Alsabti A. W., Murdin P., eds, , Handbook of Supernovae. p. 317, doi:10.1007/978-3-319-21846-5\_37

Thomas R. C., Nugent P. E., Meza J. C., 2011, *PASP*, **123**, 237

van Baal B. F. A., Jerkstrand A., Wongwathanarat A., Janka H.-T., 2023, *MNRAS*, **523**, 954

van Baal B. F. A., Jerkstrand A., Wongwathanarat A., Janka H.-T., 2024, *MNRAS*, **532**, 4106

Vartanyan D., Burrows A., Teryoshin L., Wang T., Kasen D., Tsang B., Coleman M. S. B., 2025a, *arXiv e-prints*, p. arXiv:2509.16314

Vartanyan D., Tsang B. T. H., Kasen D., Burrows A., Wang T., Teryoshin L., 2025b, *ApJ*, **982**, 9

Verner D. A., Ferland G. J., Korista K. T., Yakovlev D. G., 1996, *ApJ*, **465**, 487

Wongwathanarat A., Müller E., Janka H.-T., 2015, *A&A*, **577**, A48

Wooden D. H., Rank D. M., Bregman J. D., Witteborn F. C., Tielens A. G. G. M., Cohen M., Pinto P. A., Axelrod T. S., 1993, *ApJS*, **88**, 477

This paper has been typeset from a  $\text{\TeX}$ / $\text{\LaTeX}$  file prepared by the author.